A kinematically distorted flux rope model for magnetic clouds

M. J. Owens,[1] V. G. Merkin,[1] and P. Riley[2]

Received 6 October 2005; revised 17 November 2005; accepted 20 December 2005; published 17 March 2006.

[1] Constant-α force-free magnetic flux rope models have proven to be a valuable first step toward understanding the global context of in situ observations of magnetic clouds. However, cylindrical symmetry is necessarily assumed when using such models, and it is apparent from both observations and modeling that magnetic clouds have highly noncircular cross sections. A number of approaches have been adopted to relax the circular cross section approximation: frequently, the cross-sectional shape is allowed to take an arbitrarily chosen shape (usually elliptical), increasing the number of free parameters that are fit between data and model. While a better ''fit'' may be achieved in terms of reducing the mean square error between the model and observed magnetic field time series, it is not always clear that this translates to a more accurate reconstruction of the global structure of the magnetic cloud. We develop a new, noncircular cross section flux rope model that is constrained by observations of CMEs/ICMEs and knowledge of the physical processes acting on the magnetic cloud: The magnetic cloud is assumed to initially take the form of a force-free flux rope in the low corona but to be subsequently deformed by a combination of axis-centered self-expansion and heliocentric radial expansion. The resulting analytical solution is validated by fitting to artificial time series produced by numerical MHD simulations of magnetic clouds and shown to accurately reproduce the global structure.

Citation: Owens, M. J., V. G. Merkin, and P. Riley (2006), A kinematically distorted flux rope model for magnetic clouds, *J. Geophys. Res.*, *111*, A03104, doi:10.1029/2005JA011460.

1. Introduction

[2] Coronal mass ejections (CMEs) are huge expulsions of solar plasma and magnetic field through the corona and out into the heliosphere. CMEs are known to be the major cause of severe geomagnetic disturbances [e.g., *Cane and Richardson*, 2003], making them of critical importance to space weather studies. Remote measurements of CMEs, notably coronagraph observations (e.g., the Large Angle Spectroscopic Coronagraph) [*Brueckner et al.*, 1995] have highlighted both the event to event variability in CME size, speed, and morphology [*St. Cyr et al.*, 2000] and the lack of a single, coherent picture of the processes driving eruption [e.g., *Linker et al.*, 2003; *Antiochos et al.*, 1999; *Chen*, 1996]. The interplanetary manifestations of CMEs (ICMEs) allow the only in situ sampling of ejecta magnetic fields and plasma. Thus ICME observations and modeling can provide valuable information about the magnetic configuration and orientation of ejecta which may prove key in constraining theories of CME initiation, as well as aiding our understanding of the evolution of ejecta during their transit from the Sun to 1 AU.

[3] Magnetic clouds (MCs) are a subset of ICMEs, comprising somewhere between a quarter and a third of all ejecta [*Cane and Richardson*, 2003]. They are characterized by a smooth magnetic field rotation and enhanced magnetic field magnitude, coupled with a reduced proton temperature [*Burlaga et al.*, 1981]. The field rotation has been attributed to a magnetic flux rope (MFR) and successfully modeled as a constant-α force-free magnetic flux rope (CαMFR) [*Lundquist*, 1950; *Burlaga*, 1988; *Lepping et al.*, 1990], enabling the single-point measurements to be interpreted in terms of the large-scale structure of the magnetic cloud. This approach has proved highly productive: the local orientation of the MC (i.e., the axis of the flux rope) and its helicity can be estimated, allowing comparisons with remote observations of filament orientations and handiness, resulting in the discovery of solar cycle and hemispheric trends in the Sun's behavior [*Bothmer and Schwenn*, 1998; *Mulligan et al.*, 1998], whereas the MC radius and axial magnetic field strength can put constraints on the closed flux introduced into heliosphere by an ejection.

[4] A major shortcoming of CαMFR models is the intrinsic assumption of cylindrical symmetry. There are a number of reasons to believe that MCs have highly noncircular cross sections. Observationally, the shock standoff distance ahead of fast-moving MCs is too large to be created by a cylindrical obstacle to the flow [*Russell and Mulligan*,

[1]Center for Space Physics, Boston University, Boston, Massachusetts, USA.
[2]Science Applications International Corporation, San Diego, California, USA.

Copyright 2006 by the American Geophysical Union.
0148-0227/06/2005JA011460$09.00

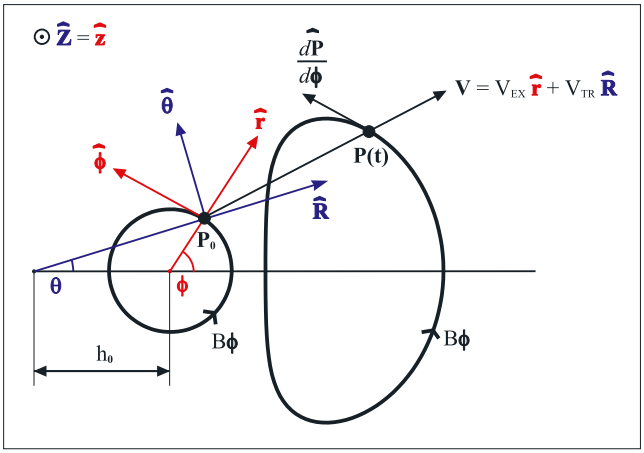

Figure 1. A schematic representation of the geometry used to generate the kinematically distorted flux-rope model. A constant-α force-free flux rope is initially located at a heliocentric height h_0. Each point within the flux-rope then moves subject to two velocities: antisunward at speed V_{TR}, and antiaxially (i.e., in the $\hat{\mathbf{R}}$ direction) at a speed V_{EX}. The intensity of the axial and nonaxial magnetic field components are assumed to remain unchanged.

2002], and the angle of the deflected solar wind flow in the sheath region ahead of such ejecta also suggests an elongated structure [Owens and *Cargill*, 2004b]. Modeling of ICMEs, both by means of simple numerical simulations [*Riley and Crooker*, 2004] and more detailed magnetohydrodynamic (MHD) simulations [*Riley et al.*, 2004], results in MC cross sections being highly oblate at 1 AU. Noncircular cross section MC models have been developed to address this issue. *Mulligan and Russell* [2001] developed an elliptical cross section model by generalizing a CαMFR model. *Hu and Sonnerup* [2001] assume that magnetic clouds can be approximated as axis-symmetric, magnetostatic structures, enabling the reconstruction of the cross-sectional shape using the Grad-Shafranov technique. This approach requires the axis orientation to be determined by minimum variance analysis (MVA) [*Sonnerup and Cahill* 1967]. *Hidalgo et al.* [2002] relaxed the force-free condition by relating the magnetic field structure of the cloud to the current density and solved the resulting equations assuming elliptical cross section geometry [see also *Hidalgo*, 2003, 2005]. Thus the general approach has been to relax the restrictions on the cross-sectional shape and thus fit an increased number of free model parameters to the data. While this increase in the number of degrees of freedom will undoubtedly lead to a better "fit" in terms of the mean square error (MSE) between the model and observed time series, it does not necessarily lead to a more accurate reconstruction of the global geometry and properties of the MC [e.g., *Riley et al.*, 2004]. In this study we attempt to relax the circular cross section approximation but in a way consistent with the physics of MCs.

2. Model

[5] We begin by assuming that somewhere in the low corona, a magnetic cloud can be approximated as a CαMFR (we are unconcerned whether the flux rope existed prior to the eruption or formed during the eruption). Despite the evidence against circular cross section MFRs at 1 AU, there are reasons to believe they are a relatively common feature of ejecta in the low corona. LASCO observations of CMEs frequently exhibit circular structures attributed to MFRs [*Low*, 1994; *Rust*, 1994; *Dere et al.*, 1999], and MHD simulations based upon a variety of initiation mechanisms [e.g., *Antiochos et al.*, 1999; *Linker et al.*, 2003; *Amari et al.*, 2000] produce approximately circular cross section MFRs in the early life of ejecta.

[6] The initial MFR is characterized by the same basic parameters that are fit to observations at 1 AU: radius (r_0, in kilometers), axial field strength (B_0, in nT), α, and helicity (H, with +1 and −1 signifying right- and left-handed helicity, respectively). Thus in axis-centered cylindrical polar coordinates $\left(\hat{\mathbf{r}}, \hat{\phi}, \hat{\mathbf{z}}\right)$, with $\hat{\mathbf{z}}$ aligned to the axis of the MFR, the magnetic field is described by

$$\mathbf{B} = HB_0J_1(\alpha r)\hat{\phi} + B_0J_0(\alpha r)\hat{\mathbf{z}}, \tag{1}$$

where $0 <= r <= r_0$ and $0 <= \phi < 2\pi$, and J_0 and J_1 are Bessel functions of the zeroth and first order. Note that $\alpha r = 2.408$ corresponds to a completely poloidal field (i.e., no axial ($\hat{\mathbf{z}}$) component), which is conventionally considered to be the MFR outer boundary.

[7] At time $t = 0$, the MFR is assumed to be at a heliocentric height h_0. Note that r_0 and h_0 define the initial angular extent of the CME: $r_0 = 1\ R_S$ and $h_0 = 2\ R_S$ translate to a width of 60° (see also Figure 1). Thus in heliocentric cylindrical polar coordinates $\left(\hat{\mathbf{R}}, \hat{\theta}, \hat{\mathbf{Z}}\right)$, with $\hat{\mathbf{Z}}$ aligned to the axis of the MFR, a point P_0 (r, ϕ, z) inside the initial MFR is given by

$$P_0(P_R, P_\theta, P_Z) = \left(\left([r\sin(\phi)]^2 + [h_0 + r\cos(\phi)]^2\right)^{1/2}, \arctan\left(\frac{r\sin(\phi)}{h_0 + r\cos(\phi)}\right), z\right). \tag{2}$$

We now consider the evolution of this structure. As the flow momentum of the solar wind far exceeds the magnetic pressure at heliocentric distances beyond a few solar radii, we ignore magnetic forces, in a similar manner to *Riley and Crooker* [2004]. We assume two separate motions of all points within the MFR: antisunward transit at a speed V_{TR}, as is undergone by the ambient solar wind, and self-expansion of the MFR driven by internal pressure forces. The linearly declining speed profiles observed in magnetic clouds at 1 AU [*Owens et al.*, 2005] suggests the expansion speed varies linearly with distance from the axis of the cloud (r/r_0). Thus the total velocity (V) of any point of within the MFR is then given by

$$\mathbf{V} = V_{TR}\hat{\mathbf{R}} + \frac{V_{EX}r}{r_0}\hat{\mathbf{r}}, \tag{3}$$

where V_{EX} is the expansion speed at the outer boundary of the magnetic cloud. Hence at a time t (in seconds), the

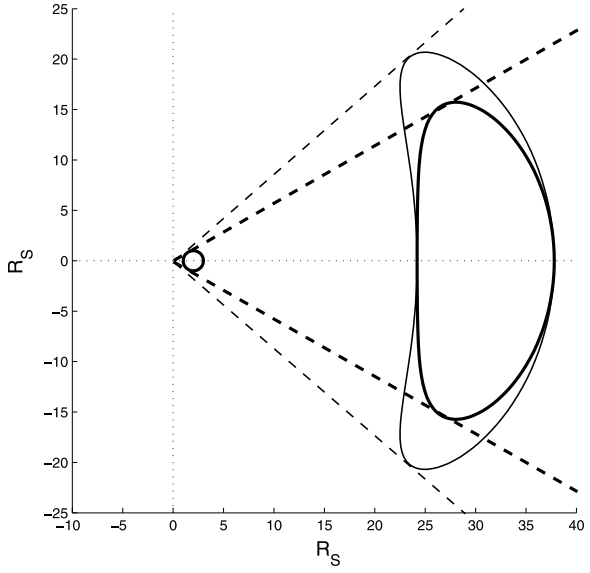

Figure 2. The cross-sectional evolution of a MFR with time, assuming full self-expansion (the thin line), and self-expansion limited to the $\hat{\mathbf{R}}$ direction (the thick line). Note that by the time the MFR has reached 30 R_S (i.e., the field of view of LASCO), full expansion produces an increase in the angular extent of the MFR cross section of ~55°. Limiting self-expansion to the $\hat{\mathbf{R}}$ direction maintains the width of the MFR cross section, as is observed.

plasma originally at point P_0 will be at point P (P_R,P_θ, P_Z), given by

$$P_R = P_R(t=0) + tV_{TR}\left(1 + \frac{Ar}{r_0}\cos(\phi-\theta)\right)$$
$$P_\theta = P_\theta(t=0) + tV_{TR}\left(\frac{Ar}{r_0}\sin(\phi-\theta)\right), \quad (4)$$

where A is the ratio of V_{EX} to V_{TR}. For observations of both magnetic cloud and noncloud ICMEs at 1 AU, *Owens et al.* [2005] found $A \sim 0.15$.

[8] The thin line in Figure 2 shows the solutions of equation (4) for $r = r_0$ and $0 <= \phi < 2\pi$ (i.e., the outer boundary of the MFR) at increasing times, using $A = 0.2$, V_{TR} = 400 km/s, $h_0 = 2R_S$, and $r_0 = 1R_S$. The cross section of the MFR becomes highly noncircular after a few solar radii, as was shown numerically by *Riley and Crooker* [2004]. Note that due to the nonzero expansion speed, the angular extent of the MFR increases with time. Coronagraph observations of limb CMEs have found the angular width of ejecta to remains constant as the CME propagates through the corona [*St. Cyr et al.*, 2000; *Schwenn et al.*, 2005]. Furthermore, in situ observations of ICMEs at 1 AU should exhibit large (~100 km/s) nonradial flow speeds within the body of the ejecta that are systematically orientated by the spacecraft intersection position, which has not been observed [e.g., *Owens and Cargill*, 2004b]. Thus we limit the expansion velocity to the $\hat{\mathbf{R}}$ direction, yielding a corrected version of equation (4):

$$P_R = \left([r\sin(\phi)]^2 + [h_0 + r\cos(\phi)]^2\right)^{1/2} + tV_{TR}\left(1 + \frac{Ar}{r_0}\cos(\phi-\theta)\right)$$
$$P_\theta = \arctan\left(\frac{r\sin(\phi)}{h_0 + r\cos(\phi)}\right) \quad (5)$$

[9] The thick line plot in Figure 2 shows the solution of equation (5) for $r = r_0$ and $0 <= \phi < 2\pi$ (i.e., the outer boundary of the MFR). The angular extent of the MFR cross section now remains constant with time, and the flow velocity within the ICME is expected to be purely radial.

[10] If we assume the magnetic field intensity contained in the poloidal and axial directions is constant (for the magnetic cloud fit we are concerned only with the direction of the magnetic field: see section 3), the magnetic field vector at a point (R, θ, z) at a time t is then simply a combination of the axial and poloidal components. The axial component is always directed along $\hat{\mathbf{Z}}$, while the poloidal component is in the (R, θ) plane, directed along the tangent to the surface of constant r (see also Figure 1):

$$\mathbf{B}\left(\hat{\mathbf{R}},\hat{\theta},\hat{\mathbf{Z}}\right) = HB_0J_1(\alpha r)\frac{\partial\hat{\mathbf{P}}}{\partial\phi} + B_0J_0(\alpha r)\hat{\mathbf{Z}}$$
$$= HB_0J_1(\alpha r)\left(\frac{-h_0 r\sin(\phi)}{\left[h_0^2 + 2rh_0\cos(\phi) + r^2\right]^{1/2}} - \frac{tV_{EX}h_0 r[h_0 + r\cos(\phi)]\sin(\phi-\theta)}{r_0\left[h_0^2 + r^2 + 2h_0 r\cos(\phi)\right]}\right)\hat{\mathbf{R}}$$
$$+ HB_0J_1(\alpha r)\left(\frac{r[r + h_0\cos(\phi)]}{h_0^2 + 2h_0 r\cos(\phi) + r^2}\right)\hat{\theta} + B_0J_0(\alpha r)\hat{\mathbf{Z}}, \quad (6)$$

where $\mathbf{P} = P_R\hat{\mathbf{R}} + P_\theta\hat{\theta}$. This equation only has a real solution if the point (R, θ, Z) is within the MFR boundary at time t (i.e., there exists a solution at time t for $0 \le r \le r_0$ and $0 \le \phi \le 2\pi$). Figure 3 shows the solution of equation (5) at a number of points in the (R, θ) plane, for a given set of parameters ($h_0 = 2\ R_S$, $r_0 = 1\ R_S$, $\alpha = 2.408$, $B_0 = 15\ nT$, $H = +1$, and $A = 0.15$) at a time when the leading edge reaches a heliocentric distance of $215R_S$. Blue dots represent points where there is no physical solution at this time, whereas the red lines show the instantaneous magnetic field vector at that point in space. The black curves are contours of constant r, the outermost contour being the magnetic cloud boundary. The solid black line shows a closest approach of half the magnetic cloud's angular extent (see also Figure 5). The next section will outline how this new magnetic field model can be fit to in situ observations of magnetic clouds (i.e., magnetic field time series).

3. Fitting the Model

[11] As with most magnetic cloud models, a "best fit" to the data is achieved by varying the free parameters so as to minimize the difference (in terms of either MSE or χ^2) between the model and observed magnetic field time series.

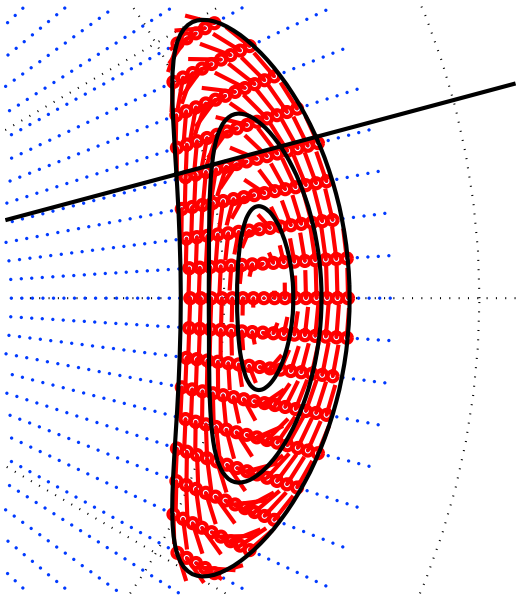

Figure 3. The magnetic field solution (i.e., equation (5)) at a number of points in the (R, θ) plane, for a given set of parameters ($h_0 = 2\ R_S$, $r_0 = 1\ R_S$, $\alpha = 2.408$, $B_0 = 15\ nT$, $H = +1$, and $A = 0.15$) at a time when the leading edge reaches a heliocentric distance of $215 R_S$. The small blue dots represent points were there is no physical solution, whereas the short red lines show the magnetic field vector at that point in space. The solid black curves are contours of constant r, the outermost contour being the magnetic cloud boundary. The solid black line shows a closest approach of half the magnetic cloud's angular extent (see also Figure 5).

We first outline the procedure used to generate the appropriate model time series.

[12] The heliospheric position (**S**) at which the observing spacecraft intercepts the magnetic cloud can be expressed in terms of the heliocentric distance, R ($\sim$215 R_S for spacecraft at L1), and the angle relative to the MFR axis, θ (see Figure 1), which is determined by the closest approach of the spacecraft to the axis (Y):

$$\theta = Y|\theta_{MAX}| = Y\arctan\left(\frac{r_0\arccos\left(\frac{-r_0}{h_0}\right)}{h_0 - \frac{r_0^2}{h_0}}\right), \qquad (7)$$

where θ_{MAX} is the heliocentric angle between the axis of the flux rope and its cross-sectional boundary (i.e., half the angular extent of the MFR).

[13] Thus the start and end times of a magnetic cloud encounter at **S** are obtained by solving equations (7) and (5) with $\mathbf{P}(t) = \mathbf{S}$ for a given set of free parameters, with $r = r_0$. Note that any arbitrary value of V_{TR} can be used to produce the same structure at a given heliocentric distance (though obviously at differing times), it is A (the ratio of transit to expansion speeds) that determines the resulting magnetic cloud morphology (see Figure 4). The model start and end times are then scaled to coincide with the observed boundaries of the magnetic cloud (t_S and t_E). For each observational data point within the cloud, the R and θ components of equation (5) are solved for r and ϕ, and equation (5) is used to calculate the corresponding model magnetic field vector for a given set of free parameters. This is then converted to the coordinate system of the observed data, nominally Geocentric Solar Ecliptic (GSE), and then transformed for the required axis orientation: ϕ_{AXIS} is the ecliptic clock angle from x_{GSE} of the MFR axis, θ_{AXIS} is the angle of the axis out of the ecliptic. Thus for a MFR axis along y_{GSE}, $\phi_{AXIS} = 90°$ and $\theta_{AXIS} = 0°$.

[14] Note that to obtain the model time series, the MFR is evolved in time and the magnetic field vector at a fixed position in the heliosphere is recorded, rather than taking a radial cut of the model taken at a fixed time (as is frequently done with simple, nonexpanding CαMFR models). Figure 5 shows that the model magnetic field time series can differ substantially when obtained by temporal evolution and radial cut methods.

[15] In order to estimate the best-fit free parameters, a simplex search method [*Lagarias et al.*, 1998] is used to minimize the difference between model and observed mag-

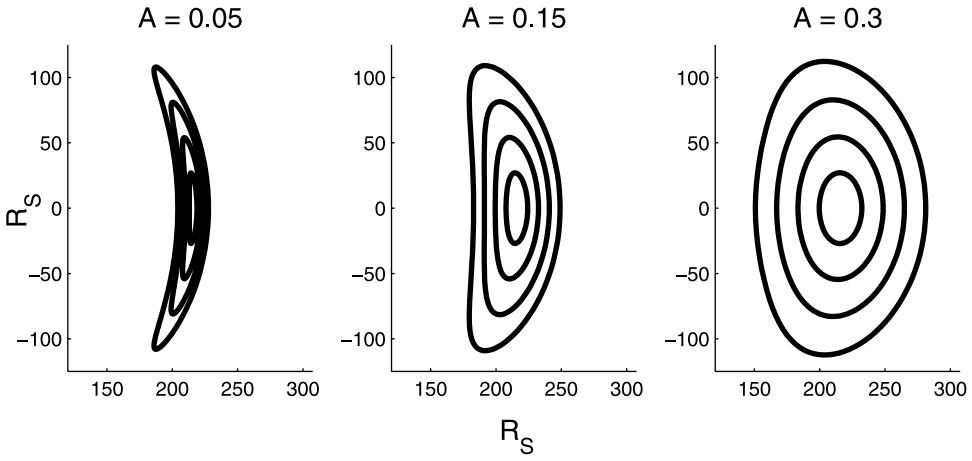

Figure 4. The 1 AU morphology of a flux-rope initially at a height of 2 R_S and with a radius of 1 R_S, for varying values of A (the ratio of the expansion to transit speeds).

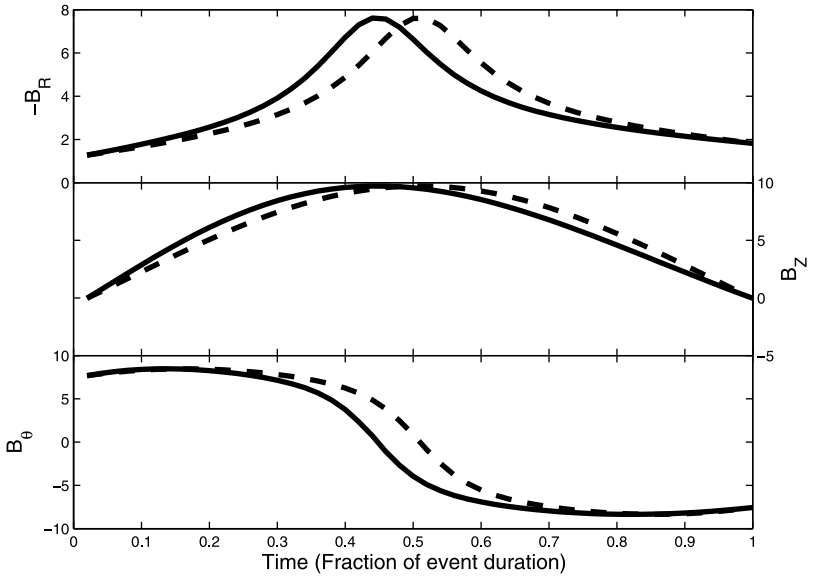

Figure 5. Model time series for a flux rope with parameters $h_0 = 2\ R_S$, $r_0 = 1\ R_S$, $\alpha = 2.408$, $B_0 = 15\ nT$, $H = +1$, and $A = 0.15$, at a heliocentric distance $R = 215R_S$ and closest approach parameter $Y = 0.5$ (i.e., the black line in Figure 3). The -R, Z, and θ components of **B** are shown; for a flux rope with its axis directed along y_{GSE}, these directions correspond to x_{GSE}, y_{GSE}, and z_{GSE}, respectively. The dashed line shows the time series obtained by taking a radial cut through the MFR at a fixed time, whereas the solid lines are for the MFR evolving in time past a fixed point (as is obtained from in situ observations). The time series have been scaled to produce events with the same duration.

netic field time series. As the computation time can be long and frequently only the local minima is located, it is important to start with reasonable initial values for the free parameters. We use MVA to make an initial estimate of the axis orientation (the axis is assumed to be along the intermediate variance direction [e.g., *Bothmer and Schwenn*, 1998]). We then use the maximum variance magnetic field (B_{MAX}) to estimate the helicity of the flux rope: a positive to negative (negative to positive) rotation of B_{MAX} indicates a right-handed (left-handed) helicity. The average value of B_{MAX} over the initial and final thirds of the magnetic cloud duration are used to systematically estimate H. If H cannot be determined in this manner, we attempt fits using both $H = +1$ and $H = -1$. The closest approach of the spacecraft to the axis (Y) is approximated by the fraction of the total magnetic field strength contained in the minimum variance component (see *Owens and Cargill* [2004b] for more details). The mean value of $|\mathbf{B}|$ over the magnetic cloud duration is used as the initial value of B_0. We fix h_0 at 2 R_S and make an initial guess of $r_0 = 1\ R_S$; α is fixed at 2.408, and an initial value of 0.15 is used for A.

[16] It was noted by *Riley et al.* [2004] that a major issue with fitting magnetic cloud models is the correct identification of the event boundaries within the observational data. For this reason, the temporal bounds of the magnetic cloud (t_S and t_E) can also be made free parameters of the fitting process (an "adaptive boundary fit"). The initial values and acceptable limits of t_S and t_E must still be determined by the observer by conventional methods. The adaptive boundary fit is of most use when the start or end times of the ICME are not well defined.

[17] In practice, the fit to data is performed in two stages: first, the χ^2 value between the observed and model magnetic field time series is minimized with r_0, θ_{AXIS}, ϕ_{AXIS}, Y, and A as free parameters (plus t_S and t_E for adaptive fits), and B_0 fixed at its initial value. Thus the fit is made only to the magnetic field direction (as is performed by *Lepping et al.* [1990] for CαMFR fits), not the magnitude. This has the two-fold advantage of reducing the number of free parameters for a single minimization cycle, and lessening the effect of ICME compression via ambient solar wind interaction, which our simple kinematic model does not account for. The axial magnetic field strength is then estimated by a second minimization of the MSE between the observed and model magnetic field components, with r_0, θ_{AXIS}, ϕ_{AXIS}, Y, and A fixed at their optimal values and B_0 as the sole free parameter. Table 1 summarizes the fixed and free parameters, along with their initial and acceptable range of values.

[18] It should be noted that even using the simplex search method with best estimates for the starting parameters, the located minimum is not always the global minimum. For this reason it is sometimes necessary to try an ensemble of starting parameters to find the best fit solution.

4. Model Validation

[19] The new magnetic cloud model is validated using MHD-simulated results, rather than observational data for two reasons: first, when fitting a magnetic cloud model to time series data, a better "fit" (in terms of reducing the mean square error between the model and observed magnetic field time series) does not necessarily translate to a better reconstruction of the large-scale orientation or morphology. With in situ observations there is no means of independently assessing how close a model fit is to the underlying "truth." However, with an MHD simulation of a

Table 1. Fixed and Free Parameters (and Their Initial and Acceptable Ranges of Values) Used to Fit the Model to Observed Data

Parameter	Initial Value	Acceptable Range of Values
	Free Parameters	
r_0	1 R_S	$0.01 < r_0 < 2\ R_S$
θ_{AXIS}	From MVA	$-pi/2 <= \theta_{AXIS} < pi/2$[a]
ϕ_{AXIS}	From MVA	$0 <= \phi_{AXIS} < 2pi$[a]
Y	From $<B_{MIN}>$	$-1 < Y < 1$
A	0.15	$0 < = A < = 1$
t_S[b]	Set by observer	Set by observer
t_E[b]	Set by observer	Set by observer
B_0[c]	From $<\|\mathbf{B}\|>$	$0 < B_0 < 1000\ nT$
	Fixed Parameters	
H[d]	Determined by rotation of B_{MAX}	
R	Heliocentric distance of observing s/c	
h_0	2 R_S	
α	2.408	

[a]The axis orientation is additionally constrained such that it must make an angle >= 5° with $\pm x_{GSE}$.
[b]For adaptive boundary fits the start and end times of the magnetic cloud are free parameters, with limits on their acceptable values set by the observer.
[c]B_0 is fixed in the initial minimization, with the best fit value determined by a second, independent minimization.
[d]If H is undetermined by B_{MAX}, fits using both helicities are attempted, and the best fit used.

magnetic cloud the global structure is known, allowing direct comparison with the model reconstructed morphology/geometry. Second, *Riley et al.* [2004] recently used such an MHD simulation of a magnetic cloud to produce artificial in situ time series and hence test many of the current MC models. By using the same test cases, the validity of this new model can be put in context of a variety of existing MC reconstruction techniques.

[20] Figure 6, adapted from *Riley et al.* [2004], shows the MHD-simulated magnetic cloud at 1 AU, with the observing "spacecraft" positions used to create the artificial time series indicated. For details of the simulation, see *Riley et al.* [2004]. The ejecta at 1 AU is highly elongated, with an aspect ratio (i.e., the ratio of the radial thickness to arc length of the "major axis") of ~5–6. For a spacecraft at point A the magnetic cloud is intercepted near the axis; the spacecraft passes just "above" the axis relative to the axis magnetic field direction (into the page). At point B the spacecraft makes a "glancing blow" of the magnetic cloud (at the "lower" edge relative to the axis field). In both cases, all the tested models predicted the correct magnetic helicity of the flux rope. Using time series A, the various models accurately reproduce the MFR orientation (i.e., to within ~10°) and the closest approach. However, with time series B all estimates of the axis orientation are off by ≥40°, though a common problem was the location of the MC boundaries. We note that in both cases all the models predict almost circular cross-sectional structures (i.e., aspect ratios close to unity) and thus would severely underestimate the flux content.

[21] In this study we have the advantage of knowing approximately where the MC boundaries are located, whereas the other modeling groups performed the fits blind. However, while this influences our choice of the initial guess of the boundaries, we perform adaptive boundary fits, allowing the model to ultimately define their position.

[22] Figure 7 shows the best fits obtained to time series A and B. The time series of the magnetic field angles (in GSE coordinates) are shown (the *Riley et al.* [2004] simulated time series are shown by solid black lines and the best model fit as solid red lines). Table 2 lists the best fit quantities for the axis orientation, closest approach param-

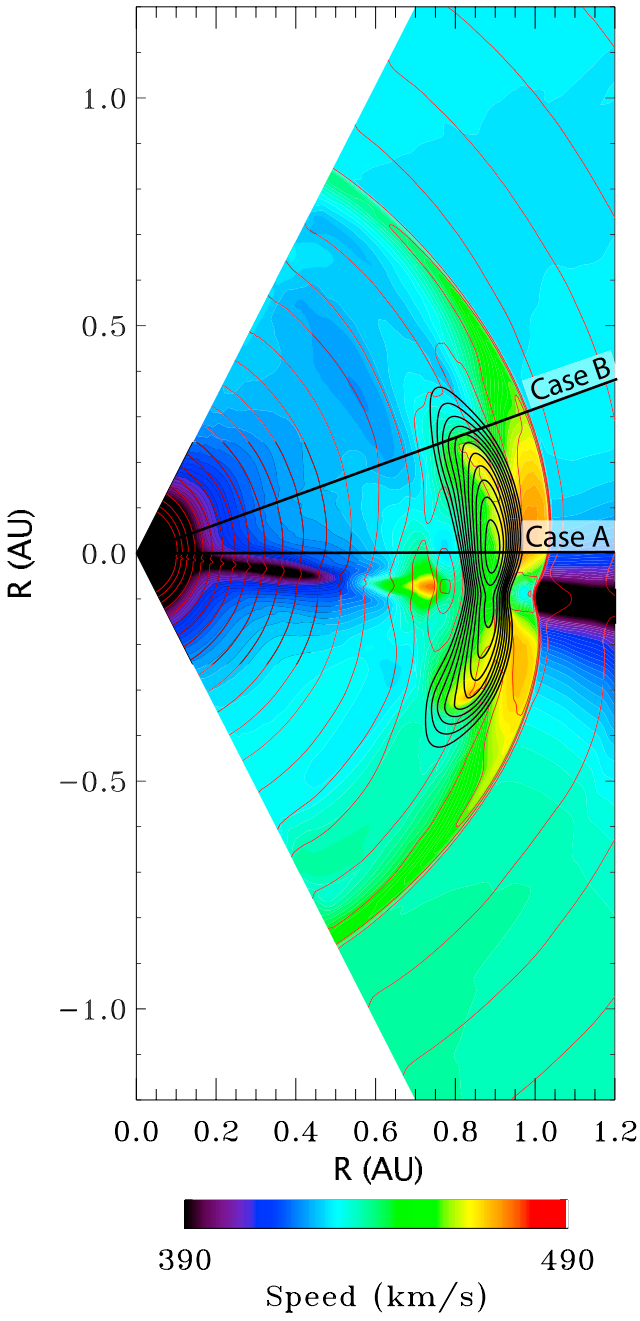

Figure 6. Figure adapted from *Riley et al.* [2004]. The numerical-MHD simulated magnetic cloud at the time when the leading edge arrives at 1 AU. The axial magnetic field vector is into the page; note the highly elongated shape of the magnetic cloud's cross section. Time series of the magnetic field and plasma properties were generated by evolving the structure past "spacecraft" at points A and B.

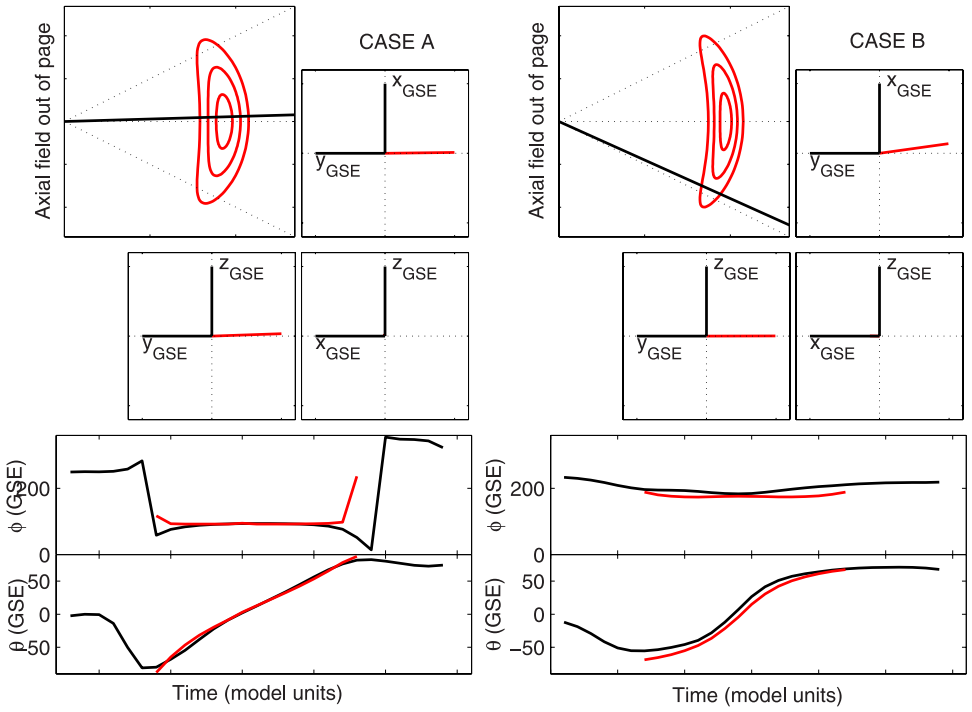

Figure 7. The best model fit (red) to MHD simulation generated time (black) series at points A and B. In both cases the model predicted and "observed" time series of the two magnetic field angles (θ and ϕ) show good agreement (bottom two panels. Time is in arbitrary model units, and hence not shown). The four square panels show the model reconstructed axis orientation and cross-sectional shape of the MC, along with the point of interception relative to the axis magnetic field (out of the page in both cases). See also Table 2.

eter and aspect ratio (determined by r_0 and A), along with their "true" values to enable direct comparison. The model-reconstructed orientation and morphology of the magnetic cloud is very accurate, for both the axis encounter (case A) and the glancing blow (case B). Note that for the axis encounter (case A), the magnetic field profile is very similar to that of a circular cross section flux rope, and hence the extent of the elongation is poorly determined relative to that of the off-axis encounter (case B). However, the axial orientation is better determined for case A than case B, as was found for the existing magnetic cloud models. We also note that the failure of the model to capture the downturning of the ϕ component of the magnetic field near the magnetic cloud boundaries caused by its interaction with the heliospheric current sheet (see Figure 6 and *Riley et al.* [2004] for more details) does not affect the ability of the model to reconstruct the global properties.

5. Discussion

[23] In this study we have demonstrated a modification to the constant-α force-free flux rope model of magnetic clouds that allows for the non-force-free elongation of the MFR cross section that has been frequently been inferred, both through indirect observation and MHD simulations. The shape of the initially circular MC cross section is only allowed to distort in accordance with the processes known to act upon it, namely heliocentric solar wind expansion and pressure-driven self-expansion. In order to obtain an analytical solution that can be routinely fit to data, magnetic forces are ignored, as is interaction with the ambient solar wind, resulting in a purely kinematic distortion as demonstrated by *Riley and Crooker* [2004].

[24] The model was validated using a numerical MHD simulation of a magnetic cloud [*Riley et al.*, 2004] and shown to accurately reproduce the large-scale structure. In particular the axis orientation was determined to within 10°, even with a highly off-axis encounter. A single spacecraft cut through a large three-dimensional structure such as a magnetic cloud will always mean the reconstruction of the global properties is somewhat ambiguous. However, we hope that this new model will allow in situ observations of magnetic clouds to be used to produce much more accurate estimates of these global properties (e.g., axis orientation, flux content, etc.) than are currently possible. Such quantities are key for linking the remote and in situ observations of ejecta and may address a number of important questions. Improved knowledge of flux rope axis orientations will determine whether a correlation exists between filament and

Table 2. Best-Fit Parameters to Time Series A and B[a]

	H	ϕ_{AXIS}	θ_{AXIS}	Y Case A(B)	Aspect Ratio[b]
True value	−1	270.0°	0.0°	∼ −0.1 (0.7)	∼ 5–6
Best-fit case A	−1	270.8°	1.9°	−0.05	3.5
Best-fit case B	−1	277.9°	0.1°	0.90	5.2

[a]The true values of the simulation results are shown for comparison.
[b]The aspect ratio of the best-fit model is determined by the free parameters A and r_0.

magnetic cloud geometry, while additionally improving our understanding about the nature of ICME force ropes; do they preexist in the corona or are they formed as a product of the eruption? Improved estimates of the flux content of magnetic clouds are critical for assessing the role of CMEs in processes such as the solar cycle variation in heliospheric flux. Furthermore, the cross-sectional shape of magnetic clouds has implications for the drag forces acting upon them [*Cargill*, 2004] and hence prediction of CME arrival times for space weather purposes [e.g., *Owens and Cargill*, 2004a].

[25] A major limitation of this kinematically distorted magnetic cloud model is the assumption that the ambient solar wind speed (V_{TR}) is constant over the initial flux rope cross section and that the flux rope does not subsequently interact with this solar wind in the heliosphere. For CMEs at solar minimum originating close to the streamer belt, the observed latitudinal variation in solar wind speed might cause the extremities of the flux rope cross section to experience a significantly higher V_{TR} than the center, which may result in ''concave-outward'' flux rope structures at 1 AU [e.g., *Odstrcil et al.*, 2004]. During such solar wind configurations it may be necessary to modify the model to incorporate a latitudinal dependence in V_{TR} via an independent solar wind speed prediction [e.g., *Arge and Pizzo*, 2000].

[26] **Acknowledgments.** This research was supported by the National Science Foundation under agreement ATM-012950, which funds the CISM project of the STC program. M.O. thanks Adam Rees of the Space and Atmospheric Physics Department, Imperial College London, for useful discussions.

[27] Shadia Rifai Habbal thanks M. A. Hidalgo and Boon-Chye Low for their assistance in evaluating this paper.

References

Amari, T., J. F. Luciani, J. J. Aly, Z. Mikic, and J. Linker (2000), Coronal mass ajection: Initiation, magnetic helicity, and flux ropes. I. Boundary motion-driven evolution, *Astrophys. J.*, *585*, 1073–1086.

Antiochos, S. K., C. R. DeVore, and J. A. Klimchuck (1999), A model for solar coronal mass ejections, *Astrophys. J.*, *510*, 485.

Arge, C. N., and V. J. Pizzo (2000), Improvement in the prediction of solar wind conditions using near-real time solar magnetic field updates, *J. Geophys. Res.*, *105*, 10,465.

Bothmer, V., and R. Schwenn (1998), The structure and origin of magnetic clouds in the solar wind, *Ann. Geophys.*, *16*, 1.

Brueckner, G. E., et al. (1995), The large angle spectroscopic coronagraph (LASCO), *Solar Phys.*, *162*, 357.

Burlaga, L. F. (1988), Magnetic clouds: Constant alpha force-free configurations, *J. Geophys. Res.*, *93*, 7217.

Burlaga, L. F., E. Sittler, F. Mariani, and R. Schwenn (1981), Magnetic loop behind and interplanetary shock: Voyager, Helios, and IMP 8 observations, *J. Geophys. Res.*, *86*, 6673.

Cane, H. V., and I. G. Richardson (2003), Interplanetary coronal mass ejections in the near-Earth solar wind during 1996–2002, *J. Geophys. Res.*, *108*(A4), 1156, doi:10.1029/2002JA009817.

Cargill, P. J. (2004), On the aerodynamic drag force acting on coronal mass ejections, *Solar Phys.*, *221*, 135.

Chen, J. (1996), Theory of prominence eruption and propagation: interplanetary consequences, *J. Geophys. Res*, *101*, 27,499.

Dere, K. P., G. E. Brueckner, R. A. Howard, D. J. Michels, and J. P. Delaboudiniere (1999), LASCO and EIT observations of helical structure in CMEs, *Astrophys. J.*, *516*, 465.

Hidalgo, M. A. (2003), A study of the expansion and distortion of the cross section of magnetic clouds in the interplanetary medium, *J. Geophys. Res.*, *108*(A8), 1320, doi:10.1029/2002JA009818.

Hidalgo, M. A. (2005), Correction to ''A study of the expansion and distortion of the cross section of magnetic clouds in the interplanetary medium,'' *J. Geophys. Res.*, *110*, A03207, doi:10.1029/2004JA010752.

Hidalgo, M. A., C. Cid, A. F. Vinas, and J. Sequeiros (2002), A non-force-free apporach to the topology of magnetic clouds, *J. Geophys. Res.*, *107*(A1), 1002, doi:10.1029/2001JA900100.

Hu, Q., and B. U. O. Sonnerup (2001), Reconstruction of magnetic flux ropes in the solar wind, *Geophys. Res. Lett.*, *28*, 1443.

Lagarias, J. C., J. A. Reeds, M. H. Wright, and P. E. Wright (1998), Convergence properties of the Nelder-Mead simplex method in low dimensions, *SIAM J. Opt.*, *9*, 112.

Lepping, R. P., J. A. Jones, and L. F. Burlaga (1990), Magnetic field structure of interplanetary clouds at 1 AU, *J. Geophys. Res.*, *95*, 11,957.

Linker, J. A., Z. Mikic, R. Lionello, P. Riley, T. Amari, and D. Odstrcil (2003), Flux cancellation and coronal mass ejections, *Phys. Plasmas*, *10*, 1971.

Low, B. C. (1994), Magnetohydrodynamic processes in the solar corona: Flares, coronal mass ejections, and magnetic helicity, *Phys. Plasmas*, *1*, 1684.

Lundquist, S. (1950), Magnetostatic fields, *Ark. Fys*, *2*, 361.

Mulligan, T., and C. T. Russell (2001), Mulitspacecraft modeling of the flux rope structure of interplanetary coronal mass ejections: Cylindrical symmetric versus nonsymmetric topologies, *J. Geophys. Res.*, *106*, 10,581.

Mulligan, T., C. T. Russell, and J. G. Luhmann (1998), Solar cycle evolution of the structure of the magnetic clouds of the inner heliosphere, *Geophys. Res. Lett.*, *15*, 2959.

Odstrcil, D., P. Riley, and X. P. Zhao (2004), Numerical simulation of the 12 May 1997 interplanetary CME event, *J. Geophys. Res.*, *109*, A02116, doi:10.1029/2003JA010135.

Owens, M. J., and P. J. Cargill (2004a), Predictions of the arrival time of Coronal Mass Ejections at 1 AU: An analysis of the causes of errors, *Ann. Geophys.*, *22*, 661.

Owens, M. J., and P. J. Cargill (2004b), Non-radial solar wind flows induced by the motion of interplanetary coronal mass ejections, *Ann. Geophys.*, *22*, 4397.

Owens, M. J., P. J. Cargill, C. Pagel, G. L. Siscoe, and N. U. Crooker (2005), Characteristic magnetic field and speed properties of interplanetary coronal mass ejections and their sheath regions, *J. Geophys. Res.*, *110*, A01105, doi:10.1029/2004JA010814.

Riley, P., and N. U. Crooker (2004), Kinematic treatment of CME evolution in the solar wind, *Astrophys. J.*, *600*, 1035.

Riley, P., J. A. Linker, R. Lionello, Z. Mikic, D. Odstrèil, M. A. Hidalgo, Q. Hu, R. P. Lepping, B. J. Lynch, and A. Rees (2004), Fitting flux-ropes to a global MHD solution: A comparison of techniques, *J. Atmos. Sol. Terr. Phys.*, *66*, 1321.

Russell, C. T., and T. Mulligan (2002), On the magnetosheath thicknesses of interplanetary coronal mass ejections, *Planet. Space Sci.*, *50*, 527.

Rust, D. M. (1994), Spawning and shedding helical magnetic fields in the solar atmosphere, *Geophys. Res. Lett.*, *21*, 241.

Schwenn, R., A. Dal Lago, E. Huttunen, and W. D. Gonzalez (2005), The association of coronal mass ejections with their effects near the Earth, *Ann. Geophys.*, *23*, 1033.

St. Cyr, O. C., et al. (2000), Properties of coronal mass ejections: SOHO LASCO observations from January 1996 to June 1998, *J. Geophys. Res.*, *105*, 18,169.

Sonnerup, B. U. O., and L. J. Cahill (1967), Magnetopause structure and attitude from Explorer 12 observations, *J. Geophys. Res.*, *72*, 171.

V. G. Merkin and M. J. Owens, Center for Space Physics, Boston University, Boston, MA 02215, USA. (mjowens@bu.edu)

P. Riley, Science Applications International Corporation, 10260 Campus Point Drive, San Diego, CA 92121, USA. (pete.riley@saic.com)